Materials Chemistry and Physics 358 (2026) 132422

Contents lists available at ScienceDirect

Materials Chemistry and Physics

journal homepage: www.elsevier.com/locate/matchemphys

Antifungal effects and mechanisms of pure metals, multi-element alloy films and nanomaterials against *Pestalotiopsis psidii*

H.K. Lin [a,*], Min-Yang Chen [a,b], Po-Wei Chang [a], Ya-Zhen Xu [b], Ying-Hong Lin [b,**]

[a] Department of Materials Engineering, National Pingtung University of Science and Technology, Pingtung, Taiwan
[b] Department Department of Plant Medicine, National Pingtung University of Science and Technology, Pingtung, 912, Taiwan

HIGHLIGHTS

- The Cu, Ag, Zn, and AgCuZn nanoparticles prepared by the laser dewetting of sputtered metal films.
- The AgCuZn nanoparticles exhibited the most potent and consistent antifungal activity.
- Their antifungal mechanism involves the rapid induction of intracellular reactive oxygen species (ROS), leading to membrane disruption, cytoplasmic leakage, and structural collapse.
- AgCuZn nanoparticles show great potential as eco-friendly alternatives to conventional fungicides.

ARTICLE INFO

Keywords:
Multi-element alloy
AlamarBlue staining
Pathogenicity test

ABSTRACT

Guava (*Psidium guajava*) is a widely cultivated tropical fruit in Asia and South America. However, it is highly susceptible to scab disease caused by *Pestalotiopsis psidii*. Reliance on conventional fungicides poses risks of resistance development, chemical residue accumulation, and environmental harm. Thus, there is a need for more sustainable alternatives. In this study, Cu, Ag, Zn, and AgCuZn coatings and nanoparticles were fabricated using physical vapor deposition and laser ablation, and their antifungal properties were evaluated. The Ag-, Zn-, and AgCuZn-based materials, whether as thin films or nanoparticles, rapidly and strongly inhibited *P. psidii* by suppressing colony growth, spore germination, and symptom expression. The nanoparticles consistently outperformed their corresponding films, suggesting that their micro-/nano-scale surface architectures enhanced their antifungal activity. In contrast, the Cu materials provided only partial inhibition and failed to prevent infection. Mechanistic assays revealed that the Ag, Zn, and AgCuZn treatments induced rapid intracellular reactive oxygen species (ROS) accumulation, leading to oxidative stress, membrane disruption, increased permeability, and cytoplasmic leakage. The treated spores exhibited severe structural damage, including collapsed cells, ruptured appendages, and extensive cytoplasmic loss, particularly after AgCuZn exposure. However, the Cu treatments did not trigger significant ROS generation or membrane injury, suggesting an alternative, possibly ion-mediated, mode of action. Overall, these findings indicate that Ag, Zn, and particularly AgCuZn nanomaterials are potent, durable antifungal agents against *P. psidii*, acting primarily through ROS-mediated cellular damage. They thus have significant potential as eco-friendly replacements for conventional fungicides in the management of guava scab disease.

1. Introduction

Guava (*Psidium guajava*), renowned for its distinctive aroma, flavor, and rich nutritional value, is extensively cultivated in Asia and South America. In Taiwan, guava is one of the most economically important fruit crops [1]. According to the Ministry of Agriculture (2023), Taiwan produced approximately 190,000 metric tons of guava in 2023, of which just under 1,900 metric tons were exported, generating an export value of around NT$100 million.

During guava cultivation, many pests and diseases threaten both

* Corresponding author.
** Corresponding author.
E-mail addresses: HKLin@mail.npust.edu.tw (H.K. Lin), pmyhlin@mail.npust.edu.tw (Y.-H. Lin).

https://doi.org/10.1016/j.matchemphys.2026.132422
Received 2 January 2026; Received in revised form 6 March 2026; Accepted 20 March 2026
Available online 23 March 2026

yield and fruit quality. Among them, guava fruit scab caused by *Pestalotiopsis psidii* is one of the most destructive. The pathogen infects fruit tissue through natural openings or wounds caused by environmental factors or insect damage, resulting in lesion formation [1]. Taiwan cultivates diverse guava varieties; however, the 'Pearl' cultivar, valued for its thick pulp, high sweetness, and flavor, is particularly vulnerable to fruit scab, which has severe consequences for yield and fruit quality. Consequently, developing effective strategies to control *P. psidii* is critical for sustaining the competitiveness of Taiwan's guava industry [2].

Currently, guava fruit scab is primarily controlled using chemical fungicides [3]. However, the prolonged use of chemical agents poses serious ecological risks, including high toxicity to aquatic ecosystems and disruption of biodiversity [4]. Moreover, repeated use of the same fungicide can prompt pathogen resistance, reducing the control efficacy and increasing production costs. Therefore, the development of safer and more environmentally friendly control strategies is essential for maintaining effective disease management while reducing chemical inputs.

Nanotechnology, a relatively young yet rapidly evolving field, has been applied across a diverse range of scientific disciplines. Within this field, metal nanoparticles (MNPs) have received particular attention because of their remarkable antimicrobial properties [5,6]. Numerous studies have demonstrated that MNPs, such as those of silver (Ag), gold (Au), copper (Cu), zinc (Zn), and aluminum (Al), can effectively inhibit the growth of pathogenic bacteria and fungi [7]. Their strong antimicrobial activity, combined with ease of functionalization and capacity to combat multidrug-resistant microorganisms, makes MNPs a promising platform for the development of novel antimicrobial strategies. For example, Ag MNPs have been reported to suppress the growth of *Fusarium solani* species complex in culture medium in a dose-dependent manner, achieving complete inhibition at 10 mg/L concentration [8].

Recent studies have further confirmed the effectiveness of Ag, Cu, and Zn nanoparticles in inhibiting the growth and reproduction of various plant pathogens [5,9–12]. Silver and copper, which are regarded as broad-spectrum antimicrobial agents [13], are increasingly used in medical and agricultural applications. However, rising concerns over the emergence of microbial resistance to these metals may compromise their long-term efficacy [14]. This indicates the need for novel strategies to enhance their applications. Zinc, an essential trace element involved in numerous biological processes [15], has likewise attracted attention for its antimicrobial potential. For instance, complexes such as thiosemicarbazones coordinated with Zn(II) exhibit pronounced antimicrobial activity [16–18], demonstrating the potential of zinc-based compounds in biomedical applications [19].

Alloy nanoparticles, which combine the properties of multiple metals, have garnered increasing interest in materials science and biomedical research [20]. Beyond binary alloys, multicomponent alloys have attracted particular attention for their enhanced stability and multifunctionality. For instance, Wang et al. [21] showed that CuAlAg, CuAlZn, and CuAlV alloy films and nanoparticles produced by laser dewetting exhibited superior thermal stability, corrosion resistance, and antimicrobial performance against human pathogens. Overall, alloy nanoparticles not only improve antimicrobial efficacy but also address the limitations associated with single-metal materials, such as rapid degradation, high cost, and risk of microbial resistance. However, despite these advantages, little is known about the antifungal potential of alloy nanomaterials against plant pathogens, particularly *Pestalotiopsis psidii*, the causal agent of guava scab disease.

To address this gap, the present study fabricated Cu, Ag, Zn, and AgCuZn coatings using physical vapor deposition, followed by laser ablation to generate nanoparticle structures. The antifungal activity of these materials was systematically evaluated against *P. psidii*, and a comparison was made between the performance of the thin films and that of the nanoparticles. In addition, mechanistic assays were performed to investigate the role of reactive oxygen species (ROS) generation, membrane disruption, and cytoplasmic leakage in pathogen inhibition. Collectively, these steps were designed to assess whether multicomponent alloy nanomaterials, particularly AgCuZn, can serve as eco-friendly alternatives to conventional fungicides for guava scab management.

2. Materials and methods

2.1. Films and nanoparticles

Using the procedures described by Wang et al. [21], single-metal (Cu, Ag, and Zn) and alloy (AgCuZn) thin films were deposited on glass substrates using a multi-target high-vacuum sputtering system (Kao Duen Tech. Co., Ltd., New Taipei City, Taiwan). The apparatus was equipped with three independent sputtering guns: two powered by direct current (DC, maximum output 1000 W) and one powered by radio frequency (RF, maximum output 400 W). A two-stage evacuation system consisting of a mechanical pump and a turbo-molecular pump was employed to achieve high-vacuum conditions with a base pressure of 5×10^{-7} Torr. During the deposition process, the flow rates of the argon (Ar) working gas and dinitrogen (N_2) reactive gas were precisely regulated via mass flow controllers (MFCs) [21].

High-purity metal targets (Ag, Cu, and Zn; purity 99.99 wt%; Ultimate Materials Tech. Co., Ltd., Hsinchu City, Taiwan) were used for film preparation. Before deposition, the glass substrates were introduced into the chamber under a working pressure of 3×10^{-3} Torr and an Ar flow of 30 sccm to remove any impurities from the substrate surface. Initial deposition trials were performed to determine the sputtering rates required to obtain 10 nm-thick coatings. In these tests, the substrate was rotated at 20 rpm to improve the thickness uniformity of the single-metal films and to ensure both the thickness and the compositional uniformity of the alloy films. The film thicknesses were measured using a D-300 surface profilometer (Alpha Step, KLA-Tencor Co., Ltd., Milpitas, USA), and the sputtering rates were calculated from the deposition time and final thicknesses. These values were then used to estimate the required durations of the main sputtering experiments. Pure metal films (Cu, Ag, and Zn; 10 nm thickness) were obtained by connecting each target to a DC power supply. The ternary alloy film ($Cu_{33}Ag_{33}Zn_{34}$) was fabricated by co-sputtering, with the Cu, Ag, and Zn targets connected to the DC1, DC2, and RF power supplies, respectively [21].

Following the sputtering process, the deposited films (pure metal and alloy) were dewetted to induce nanoparticle formation. Specifically, dewetting was performed using a G3 SM Series pulsed fiber laser (SPI Co., Ltd., UK) operating at a wavelength of 1062 ± 3 nm in the near-infrared range, with a beam diameter of ~40 μm, pulse frequency of 300 kHz, power of 8 W, scan speed of 1000 mm s^{-1}, and scan pitch of 20 μm.

2.2. Surface contact angle measurement

The surface wettability of the deposited films and particles was assessed using an OCA15EC contact angle meter (Dataphysics Co., Ltd., Filderstadt, Germany). Deionized (DI) water droplets (ddH_2O) were dispensed onto the sample surface via the built-in precision syringe of the system, and the static contact angle formed between the droplet and the solid surface was measured using the sessile drop method to evaluate the surface wettability and compare the differences among the experimental groups. Based on the measured contact angles, the surfaces were classified as hydrophilic (10°–90°), hydrophobic (90°–150°), or superhydrophobic (>150°) [22].

2.3. Preparation of guava scab pathogen

Strain PM-SSH-081 of the guava scab pathogen (*Pestalotiopsis psidii*) was obtained from the PM210 Laboratory at Pingtung University of Science and Technology in Taiwan. The terminal hyphae of the pure strain were excised and cultured in potato dextrose agar (PDA) medium

(20% potato extract, 2% agar, 2% dextrose) in preparation for subsequent experiments.

2.4. Evaluation of colony growth inhibition by plate assay

The conidia of *P. psidii* cultured for 7 days were harvested from the medium using sterile water to obtain a conidial suspension. The suspension was filtered through a 400-mesh stainless steel sieve to remove hyphal fragments and purify the resulting conidia. After filtration, a ten-fold serial dilution was performed to adjust the final concentration of the conidial suspension to 4×10^3 spores/mL. A 150 μL aliquot of the purified conidial suspension was brought into contact with the metal films and metal particles to evaluate the effects of different metallic materials on conidial colony formation. Glass substrates were used as the control group.

Contact assays were conducted for 1, 5, 10, 15, and 30 min. At each time point, 100 μL of the treated suspension was retrieved and uniformly spread on PDA plates using sterile triangular glass rods. The plates were incubated at 28 °C for 24 h, after which colony formation was observed to assess the impact of the different metal and alloy surfaces on the conidial viability. The plates were further incubated up to 48 h, during which photographic documentation was performed to analyze the colony growth characteristics and distribution under different treatment conditions.

For each sample, the antifungal effect was expressed as the inhibition rate (%), calculated as follows: $[(CK - \text{treatment}/CK)] \times 100$, where *CK* is the colony count on the glass control, and *treatment* is the colony count after contact with the as-deposited or dewetted films.

2.5. Spore germination assay

A 150 μL aliquot of the prepared conidial suspension was brought into contact with the as-deposited and laser-processed films for 15 min to evaluate the effects of the different treatments on conidial germination. Subsequently, four 10 μL droplets were taken from the treated suspension and evenly dispensed onto clean glass slides. The slides were then subjected to humidification treatment and incubated in the dark. At 0, 4, 8, 12, and 24 h post-incubation, the germination of conidia was observed using a ZEISS optical microscope (Zeiss Axioskop 2; Zeiss Co. Ltd., Fujian, China) equipped with a TCapture imaging system (Tucsen Photonics Co. Ltd., Fujian, China). The germination ability of the *P. psidii* conidia was evaluated using the spore germination rate (%), with germination defined as a germ tube length exceeding half the total length of the conidium.

2.6. Virulence assays

The surfaces of the guava fruits were first cleaned with 75% ethanol to remove any surface contaminants. The fruits were then thoroughly rinsed with sterile water to eliminate any residual ethanol, dried using sterile paper towels, and air-dried for 10 min in a sterile laminar flow cabinet. A conidial suspension at a concentration of 4×10^4 spores/mL was prepared, and 100 μL of this suspension was brought into contact with the metal films and particles for 15 min. Following treatment, three wounds with a depth of approximately 1 mm were created on the surface of each guava fruit using a sterile inoculating needle. Subsequently, 10 μL of the treated conidial suspension was inoculated onto each wound site, and the wounds were covered with Water Agar (WA) medium to maintain moisture and prevent drying out of the inoculum. After inoculation, the fruits were sealed with parafilm to maintain their water content and incubated at 28 °C for 48 h to prompt pathogen infection and lesion development. After two days, the WA medium and parafilm were removed, and lesion development was monitored daily. The lesion diameters were quantified using ImageJ 1.52t software (National Institutes of Health, Bethesda, USA) to evaluate the effects of the different treatments on guava infection by *P. psidii*.

2.7. Assessment of mitochondrial activity using Alamarblue assay

The mitochondrial activity of the *P. psidii* conidia was evaluated using the AlamarBlue Cell Viability Assay (Geno Technology, Inc., California, USA). For the assay, 100 μL of the conidial suspension was exposed to the metal films and nanoparticles for 15 min. After exposure, 50 μL of the treated suspension was mixed with 50 μL of Potato Dextrose Broth (PDB) and incubated in a shaking incubator (Lian Shen Co., Ltd., Taichung, Taiwan) under gentle agitation for 24 h. Following incubation, 90 μL of the culture was combined with 10 μL of AlamarBlue reagent and incubated at 28 °C in the dark for an additional 24 h. After staining, the absorbance of the samples was measured at 570 and 600 nm using a SPECTROstar Nano spectrophotometer (BMG LABTECH Pty Ltd., Offenburg, Germany). The AlamarBlue reduction rate was then calculated to assess the impact of the metal films and nanoparticles on the mitochondrial activity of the conidia. As a positive control for mitochondrial damage, 50 μL of autoclaved conidial suspension was mixed with 50 μL of PDB. As a negative control, 50 μL of sterile DI water (ddH_2O) was mixed with 50 μL of PDB to represent untreated, healthy conidia.

The reduction rate was calculated as

$$\text{Reduction of AlmarBlue}\ (\%) = (O2 \times A1) - (O1 \times A2) \times 100 \div (R1 \times N2) - (R2 \times N1),$$

where:

O1: molar absorptivity coefficient of oxidized AlmarBlue at 570 nm (80586)

O2: molar absorptivity coefficient of oxidized AlmarBlue at 600 nm (117216)

R1: molar absorptivity coefficient of reduced AlmarBlue at 570 nm (155677)

R2: molar absorptivity coefficient of reduced AlmarBlue at 600 nm (14652)

A1: absorbance value of test sample at 570 nm

A2: absorbance value of test sample at 600 nm

N1: absorbance value of negative control at 570 nm

N2: absorbance value of negative control at 600 nm

2.8. Assessment of cell apoptosis and membrane integrity

The apoptosis and membrane permeability of the pathogen cells were evaluated using propidium iodide (PI) fluorescent staining. In conducting the assay, 150 μL of conidial suspension was exposed to the treated samples for 15 min. After exposure, 100 μL of the treated suspension was transferred into a 1.7 mL microcentrifuge tube, and 100 μL of binding buffer was added. The mixture was gently homogenized and incubated at 4 °C in the dark for 1 h to stabilize the membrane structures and minimize background fluorescence. Following fixation, 10 μL of PI solution (5 μg/mL; Apoptosis Kit, Takara Co., Ltd., San Jose, USA) was added, and the samples were further incubated at 4 °C in the dark for 1 h to allow thorough binding of the PI to the nuclear DNA. After staining, 10 μL of the stained conidial suspension was placed on a clean glass slide. The samples were observed under a fluorescence microscope (Olympus BX53, Sage Vision Co., Ltd., New Taipei City, Taiwan) at an excitation wavelength of 535 nm to detect PI fluorescence. The microscopy images were then analyzed to assess the extent of PI binding to the conidial DNA, thereby quantifying the level of apoptosis induced by the different treatments.

2.9. Analysis of intracellular nucleic acid and protein leakage

To evaluate the release of intracellular components from the pathogen conidia after contact with the test specimens, a leakage assay was performed using the procedure described by Yan and Wu [23,24].

Briefly, 150 μL of the conidial suspension was exposed to the test

specimens for 15 min and then filtered through 90 mm qualitative filter paper (Advantec Toyo Kaisha Ltd., Tokyo, Japan) to remove any unadsorbed cells. The retained conidia were resuspended in an equal volume of DI water and incubated at room temperature for 30 min to promote the release of intracellular constituents. The supernatant (1 μL) was then placed on the sample stage of a spectrophotometer (BMG LABTECH Pty Ltd., Offenburg, Germany), and the absorbance was recorded at 260 and 280 nm. Absorbance increases at these wavelengths were taken as indicators of nucleic acid and protein leakage, thereby reflecting membrane disruption and cellular damage.

2.10. Scanning electron microscopy (SEM) observation of conidial surface morphology after material treatment

The surface morphologies of the *P. psidii* conidia after exposure to the different metal and nanoparticle surfaces were observed using ultra-high-resolution field-emission scanning electron microscopy (FESEM; JSM-7600F, JEOL Ltd., Tokyo, Japan). For preparation, 300 μL of *P. psidii* conidial suspension (1000 conidia μL^{-1}) was incubated on 2 × 2 cm^2 metal films, nanoparticle specimens, and glass slides (negative control) for 30 min. The suspensions were collected into microcentrifuge tubes and centrifuged at 13,300 rpm for 5 min to pellet the cells. The conidia were fixed in 2.5% glutaraldehyde for 2 h and washed twice with phosphate-buffered saline (PBS; diluted with deionized water) to remove excess fixative. The samples were subsequently dehydrated using a graded ethanol series (30%, 50%, 70%, 80%, 90%, and 100%), with thorough exchange at each step. After dehydration, the specimens were dried using a critical point dryer (HCP-2, Hitachi Co., Ltd., Tokyo, Japan) and then sputter-coated with metal using an ion sputter coater (HUS-SGB, Hitachi Co., Ltd., Tokyo, Japan) to enhance their conductivity. Finally, the prepared conidia were observed and imaged using FESEM to evaluate changes in their surface microstructure.

2.11. Fluorescence staining analysis of oxidative stress response of conidia after material treatment

To determine the intracellular accumulation of reactive oxygen species (ROS) in *the P. psidii* conidia following exposure to the metal surfaces, fluorescence staining was performed using the CheKine™ Mitochondrial ROS Detection Kit (KTB1911; Abbkine Scientific Co., Ltd., Georgia, USA) according to the manufacturer's instructions. Before the staining process, 150 μL of conidial suspension was incubated with the metal specimens for 15 min. Subsequently, 100 μL of the suspension (approximately 10^3 conidia) was transferred into 1.7 mL sterile microcentrifuge tubes, mixed thoroughly with 10 μL of Reagent II, and then combined with 200 μL of Reagent I for pretreatment. The resulting mixtures were kept on ice until staining.

For the staining procedure, 20 μL of the pretreated sample was transferred to a new tube as the treatment group, and 20 μL of Reagent I served as the control group. Each tube received 50 μL of Reagent III, 50 μL of Reagent IV, 50 μL of Reagent V, and 30 μL of Working Reagent VI. The tubes were then incubated at 4 °C in the dark for 1 h to allow sufficient interaction between the probe and the intracellular ROS. After staining, 10 μL of the suspension was placed on a glass slide and examined under a fluorescence microscope (Olympus BX53; Sage Vision Co., Ltd., New Taipei City, Taiwan) at an excitation wavelength of 488 nm to detect ROS-specific fluorescence signals. Variations in the fluorescence intensity were used to assess the degree of oxidative stress induced in the conidia by the different material treatments.

Analysis of variance (ANOVA) tests were conducted to determine significant differences among the groups. When the ANOVA results indicated significance, Tukey's honestly significant difference (HSD) test was applied for post hoc multiple comparisons. In addition, pairwise differences between two groups were further evaluated using independent-sample or paired-sample *t*-tests, depending on the experimental design. A threshold of $p < 0.05$ was considered statistically significant. All the analyses were performed using IBM SPSS Statistics v20.

3. Results and discussion

3.1. As-sputtered and dewetted films

The surface morphologies of the thin films and nanoparticles were examined using SEM. The results showed that all the metallic films consisted of uniform and continuous layers on the glass substrate, with an approximate thickness of 10 nm. The surfaces were smooth, with no cracks, fractures, or island-like structures, confirming that the PVD process produced stable deposition with good coverage and adhesion (Fig. 1(a)–1(d)). After the laser dewetting process, the Cu and Ag films transformed into well-defined spherical morphologies with clear edges and high roundness, although a few regions showed residual island-like metal structures owing to incomplete dewetting. Particle size analysis based on multiple-point measurements revealed that the average diameter of the Cu particles was 105.6 nm with a narrow and uniform size distribution, while that of the Ag particles was 116.8 nm (Fig. 1(e) and (f)).

In contrast, the dewetted Zn and AgCuZn films showed pronounced residual island-like structures. This suggests that the physical properties of Zn may hinder its complete melting and the formation of spherical particles during the laser-induced dewetting process. The average particle diameters of the Zn and AgCuZn particles were 187.6 nm and 176.8 nm, respectively. Overall, the results indicate that the particles in the Zn-containing systems were generally larger and less structurally uniform than those in the Cu and Ag systems, highlighting the need for further optimization of the laser dewetting process to achieve improved stability (Fig. 1(g) and (h)).

3.2. Surface contact angle measurement

The contact angles of the water droplets placed on the different surfaces showed marked differences. The contact angle of the glass control was 60.5°. By comparison, the contact angles of the droplets on the Cu, Ag, Zn, and AgCuZn films were 82.2°, 82.8°, 84.5°, and 84.9°, respectively. Although these values were significantly higher than that of glass, they remained within the hydrophilic range (<90°) (Fig. 2). The droplets placed on the dewetted films showed markedly higher contact angles than those on the thin-film counterparts. In particular, the contact angles on the Cu, Ag, Zn, and AgCuZn nanoparticle surfaces were 114.4°, 115.5°, 116.3°, and 117.1°, respectively. Although these values did not reach the superhydrophobic threshold (>150°), they were significantly higher than those of the untreated samples. This indicates that the laser dewetting process effectively altered the surface microstructure of the materials, producing nanoscale particles or textures that enhanced the surface hydrophobicity. Previous studies have reported that this hydrophobicity results mainly from an increased surface roughness and changes in the surface energy [25].

3.3. Evaluation of colony growth inhibition by plate assay

Conidial exposure to Cu thin films and Cu nanoparticles (Cu particles) for 1 min resulted in an inhibition rate of only 16–23%, which was significantly lower than that of the other treatment groups. After 5 min, the inhibitory effect remained below 30%. Although the inhibition rate increased to 60% after 5 min and further improved with prolonged contact, it remained below 100% even after 30 min, indicating that some conidia continued to grow on the culture medium. In contrast, exposure to the Ag film and nanoparticles for 1 min achieved an inhibition rate of >50%. After 10 min, the inhibition rate reached 77.1% for the Ag film and 91.9% for the Ag particles, a statistically significant difference between the two. After 15 min, the Ag particles achieved complete (100%) inhibition, while the Ag film achieved an inhibition rate of 94.6%. After

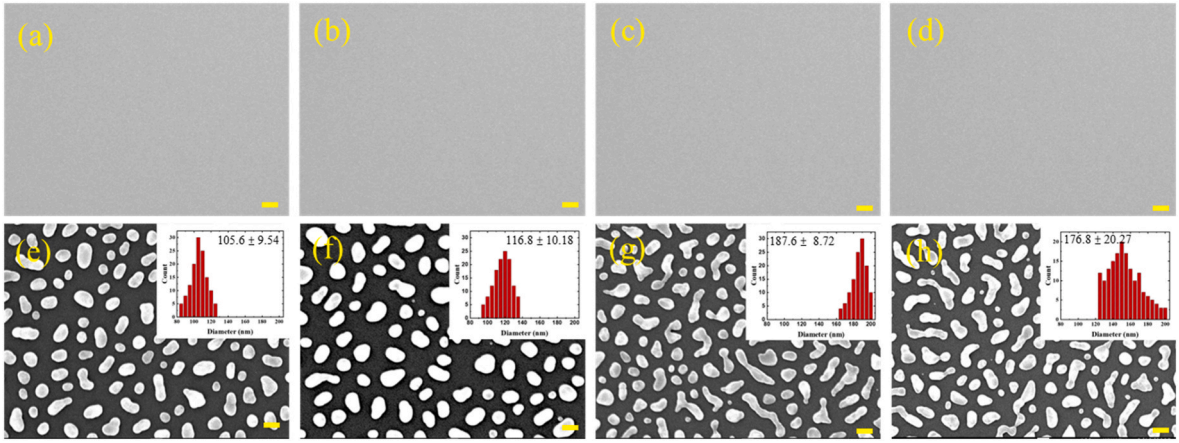

Fig. 1. Scanning electron micrographs (50,000 ×) of Cu, Ag, Zn, and AgCuZn films and nanoparticles. (a) Cu film, (b) Ag film, (c) Zn film, (d) AgCuZn alloy film, (e) Cu nanoparticles and their size distribution, (f) Ag nanoparticles and their size distribution, (g) Zn nanoparticles and their size distribution, and (h) AgCuZn alloy nanoparticles and their size distribution. Scale bar = 100 nm.

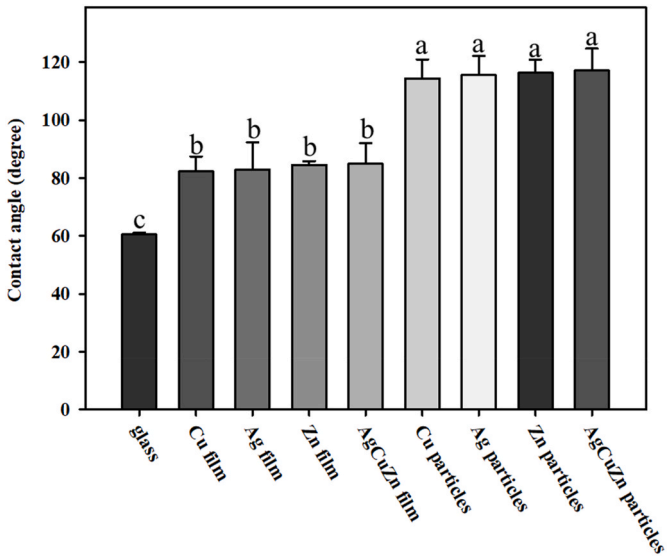

Fig. 2. Average water contact angles measured on glass, Cu, Ag, Zn, and AgCuZn films or nanoparticles. Values are expressed as mean ± standard deviation (n = 3) and were analyzed by one-way ANOVA followed by Tukey's HSD test. Columns sharing the same letter are not significantly different at $p < 0.05$.

30 min, the Ag film also reached 100% inhibition. Exposure to the Zn film and particles for 1 min resulted in >65% inhibition. After 5 min, the Zn particles achieved >90% inhibition, while the Zn film achieved 87.7%. Although this difference between them was not statistically significant, the dewetted film still showed a stronger inhibitory effect. Both surfaces reached 100% inhibition after 15 min, with no visible colony formation in either culture medium. The AgCuZn film and particles achieved inhibition rates of 65.3% and 81.9%, respectively, after 1 min, revealing a statistically significant difference in their antibacterial activity. After 5 min, the inhibition rate reached 83.1% for the AgCuZn film and 95.9% for the AgCuZn particles, with no significant difference between the two. After 15 min, both the AgCuZn film and AgCuZn particles achieved full (100%) inhibition (Fig. 3 and Table 1).

Although the nanoparticles generally exhibited greater inhibitory efficacy than the films, the Cu thin film showed higher inhibition rates than the Cu nanoparticles during the early exposure period (1–10 min). This exception highlights that thin films may provide more rapid antimicrobial action than nanoparticles in specific contexts. Such an outcome may be related to the wettability properties of the materials, as suggested by Shebl et al. [26], who reported that hydrophobic and positively charged metal nanoparticles not only damage cell membranes but also disrupt pre-formed bacterial biofilms, thereby compromising cellular protection. Moreover, micro/nanobubbles (MNBs), defined as gas bubbles with diameters in the micrometer to nanometer range, exhibit higher gas–liquid mass transfer efficiency and oxygen dissolution capacity than larger bubbles. When collapsing rapidly in large numbers, MNBs can generate substantial amounts of ROS, further enhancing the oxidative stress. It is therefore hypothesized that increased surface hydrophobicity may promote MNB generation or activity, thereby intensifying ROS accumulation and ultimately strengthening oxidative damage to pathogens, leading to improved antimicrobial efficacy [27].

3.4. Spore germination assay

In the control group, in which the conidia were exposed to glass for 15 min before incubation, the *P.* conidia exhibited germination rates of 10.1% at 4 h, 46.1% at 8 h, 73.8% at 12 h, and 85.0% at 24 h. These results indicate that the majority of germination occurred between 4 and 12 h of incubation (Fig. 4). After 15 min of exposure to the Cu films and nanoparticles, the conidial germination rates after 4 h of incubation were 13.4% and 10.8%, respectively, which were not significantly different from that of the control group. After 8 h of incubation, the germination rates reached 42.3% and 43.6%, again with no significant differences from the control. After 12 h, however, the germination rates increased to 54.0% and 54.4%, which were significantly lower than that of the control. After 24 h, the germination rates increased slightly to 59.0% and 59.1%, remaining well below the control (85.0%). The conidia exposed for 15 min to the Ag film, Zn film, AgCuZn film, and their corresponding dewetted surfaces showed a germination rate of <1% after 4 h of incubation. After 8 h, the germination rates ranged from 8.8% to 12.8%. At 12 h, the germination rates increased slightly to 15.7–19.2%, but were still significantly lower than those of the control and Cu groups. After 24 h, the germination rates remained low, ranging from 23.1% to 27.3%.

Overall, the assay results showed that both the metal thin films and the nanoparticles significantly suppressed *P. psidii* conidial germination, with the Ag, Zn, and AgCuZn treatments maintaining consistently lower germination rates than the control across both the early (4–8 h) and later (12–24 h) incubation periods. Moreover, for all the treatment groups, most conidia germinated between 8 and 12 h of incubation. The present results are thus consistent with the findings of Parveen et al. [28], who reported effective inhibition of fungal spore germination and early developmental stages.

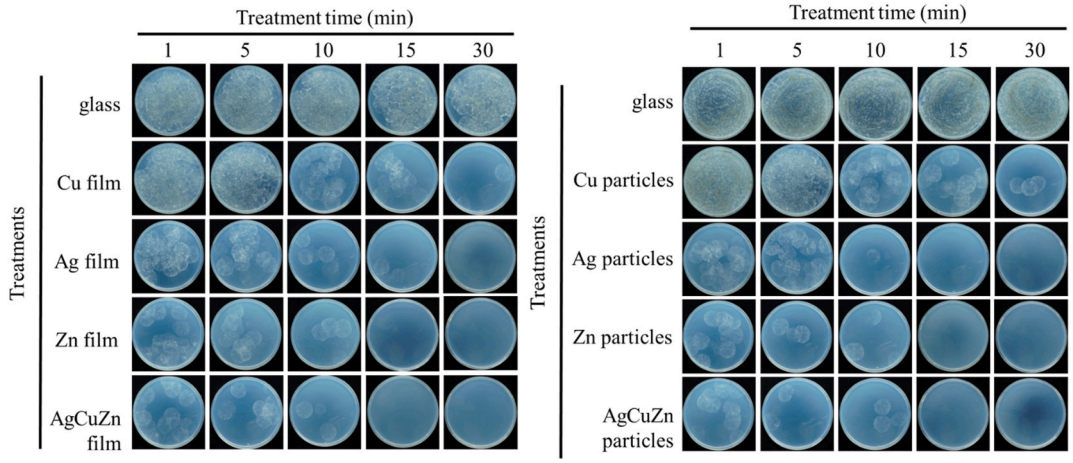

Fig. 3. Representative plate images showing colony development of *Pestalotiopsis psidii* conidial suspensions after contact with glass, Cu, Ag, Zn, and AgCuZn films or nanoparticles at various time points.

Table 1
Inhibition rates of *Pestalotiopsis psidii* spore suspensions in contact with glass, Cu, Ag, Zn, and AgCuZn films and particles for 1, 5, 10, 15, and 30 min. Values are expressed as mean ± standard deviation (n = 3) and were analyzed by one-way ANOVA followed by Tukey's HSD test. Columns sharing the same letter are not significantly different at $p < 0.05$.

	Contact time with the film (min)				
	1	5	10	15	30
Glass(CK)	-	-	-	-	-
Cu film	23.5 ± 4.7c	29.7 ± 1.8c	60.4 ± 3.1b	69.5 ± 3.2b	92.6 ± 1.0a
Ag film	52.5 ± 1.0b	60.9 ± 2.7b	77.1 ± 3.1b	94.6 ± 0.3a	100 ± 0.0a
Zn film	65.3 ± 2.7b	87.7 ± 2.8a	97.0 ± 0.3a	100 ± 0.0a	100 ± 0.0a
AgCuZn film	66.7 ± 3.9b	83.1 ± 1.7a	96.0 ± 0.6a	100 ± 0.0a	100 ± 0.0a
Cu particles	16.2 ± 0.7c	27.0 ± 2.0c	60.5 ± 1.6b	69.4 ± 2.1b	91.0 ± 1.7a
Ag particles	60.0 ± 1.9b	73.9 ± 1.1b	91.9 ± 2.2a	100 ± 0.0a	100 ± 0.0a
Zn particles	79.1 ± 3.1a	93.0 ± 1.3a	99.7 ± 0.1a	100 ± 0.0a	100 ± 0.0a
AgCuZn particles	81.9 ± 3.5a	95.9 ± 1.3a	99.6 ± 0.1a	100 ± 0.0a	100 ± 0.0a

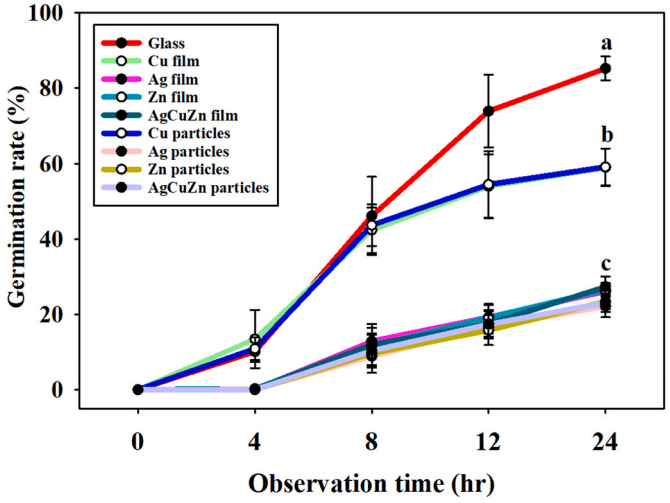

Fig. 4. Spore germination rates of *Pestalotiopsis psidii* after contact with glass, Cu, Ag, Zn, and AgCuZn thin films or nanoparticles. Values are expressed as mean ± standard deviation (n = 3) and were analyzed by one-way ANOVA followed by Tukey's HSD test. Within a given treatment group, bars that share the same letter are not significantly different ($p < 0.05$).

3.5. Virulence assays

For the glass (untreated) control sample, visible lesions were observed on the guava fruits as early as 2 days post-inoculation (dpi), with all three inoculation sites exhibiting symptoms. The mean lesion diameter reached 5.8 mm at this point and progressively expanded to an average of 40.8 mm by 7 days post-inoculation (dpi). In contrast, no visible lesions were detected on the fruits inoculated with conidia pretreated with DI (negative control) throughout the 7-day observation period. Pathogens were re-isolated from lesions on the glass control fruits at 7 dpi, and the presence of *P. psidii* conidia was confirmed microscopically, verifying that the lesions were caused by *P. psidii* rather than other microorganisms. Small necrotic spots that appeared outside the inoculation area yielded no fungal isolates and were therefore attributed to physiological rather than pathogenic injuries. The conidia exposed to Cu film and Cu particles for 15 min prior to inoculation produced visible lesions by 2 dpi, with initial mean diameters of 5.8–5.9 mm, comparable to those of the control. The lesions subsequently expanded by 7 dpi but remained smaller than those in the control, averaging 32.7 mm (Cu film) and 28.8 mm (Cu particles). Thus, the Cu particles exerted a stronger inhibitory effect on lesion expansion than the Cu film. The conidia exposed to the Ag film and Zn film showed markedly delayed disease development. For the Ag film, visible lesions were not detected until 4 dpi and showed a mean diameter of just 3.5 mm, which expanded to 6.1 mm by 7 dpi. In the Zn group, the lesions appeared even later, at 6 dpi, with a diameter of 3.4 mm, and reached only 4.5 mm by 7 dpi, indicating both a delayed onset and slower progression than the Ag film treatment. The fruits inoculated with conidia pretreated with AgCuZn film, Ag particles, Zn particles, and AgCuZn particles showed no visible lesions over the entire 7-day period. Although minor dehydration-related necrosis was observed at several inoculation points, *P. psidii* pathogen could not be identified in any of these areas. These findings demonstrate that the AgCuZn film, Ag

particles, Zn particles, and AgCuZn particles completely suppressed *P. psidii* infection under the tested conditions (Fig. 5 and Table 2).

3.6. Assessment of mitochondrial activity using Alamarblue assay

Conidia exposed to Cu film and Cu particles for 15 min were incubated with AlamarBlue reagent, and the absorbance at wavelengths of 570 nm and 600 nm was measured to calculate the reduction rate. After treatment, the reduction rate decreased from 92.5% in the control group to 85.2% and 80.1% in the Cu film and Cu particle groups, respectively. However, statistical analysis revealed no significant differences among the three groups ($p > 0.05$). In all cases, the AlamarBlue reagent changed from its oxidized, non-fluorescent blue form to a reduced, fluorescent pink form, indicating that the mitochondrial function was largely maintained. By contrast, the conidia exposed for 15 min to Ag film, Zn film, AgCuZn film, Ag particles, Zn particles, and AgCuZn particles exhibited markedly reduced AlamarBlue reduction rates, ranging from 11.5% to 8.6%. In these groups, the reagent remained in its oxidized, non-fluorescent blue state, suggesting severe impairment of the mitochondrial electron transport chain (Fig. 6).

Overall, the AlamarBlue assay demonstrated that the Cu film and particles caused only a slight, non-significant decrease in the mitochondrial activity compared to the control, whereas the Ag-, Zn-, and AgCuZn-based treatments drastically suppressed the mitochondrial reduction capacity of the cells. This finding is consistent with previous reports showing that only high concentrations of Cu nanoparticles (500 mg mL^{-1}) significantly inhibit fungal cell activity and block AlamarBlue reduction [29]. Collectively, these results suggest that Cu materials exert antifungal effects through mechanisms other than direct disruption of the mitochondrial electron transport chain, potentially involving cell membrane damage or interference with other metabolic pathways.

3.7. Assessment of cell apoptosis and membrane integrity

The conidia in the glass control, Cu film, and Cu particle groups exhibited only weak PI fluorescence, with no spores showing visible red fluorescence (Fig. 7). This finding indicates that the cell membranes remained intact and the dye was unable to penetrate the cells. By contrast, the spores treated with Ag film, Zn film, Ag particles, and Zn particles showed intense red fluorescence (green arrows), with a markedly increased stained area and fluorescence intensity compared to the control, indicating substantial membrane permeability damage. The AgCuZn film and AgCuZn particle groups not only showed strong intracellular PI fluorescence but also dispersed red signals around the periphery of the cells (blue arrows). This phenomenon suggests severe membrane rupture, leading to the extracellular release of nucleic acids (DNA and/or RNA) into the cytoplasm. Overall, the present findings show a clear distinction between the different treatments. In particular, the Ag-, Zn-, and AgCuZn-based materials markedly increased the membrane permeability of the *P. psidii* pathogen, whereas the Cu-based materials left the membranes largely intact. These results highlight the superior membrane-disruptive capacity of the Ag, Zn, and AgCuZn treatments compared with Cu and align with previous reports showing that metal films and particles disrupt the membrane potential and dynamics in *Candida albicans* in a manner similar to amphotericin B [30].

Table 2
Lesion size on guava fruits 1–7 days after inoculation with *Pestalotiopsis psidii* conidial suspensions previously exposed to glass, Cu, Ag, Zn, and AgCuZn alloy thin films or nanoparticles. Values are expressed as mean ± standard deviation (n = 3) and were analyzed by one-way ANOVA followed by Tukey's HSD test. Columns sharing the same letter are not significantly different at $p < 0.05$

Treatment	Lesion Size (mm)						
	Day 1	Day 2	Day 3	Day 4	Day 5	Day6	Day7
Glass	0	5.8 ± 0.6a	12.3 ± 0.9a	16.7 ± 1.9a	22.9 ± 2.4a	29.6 ± 2.7a	40.8 ± 3.7a
Cu film	0	5.9 ± 0.4a	12.6 ± 2.5a	16.7 ± 1.9a	21.4 ± 2.5a	28.6 ± 3.8a	32.7 ± 4.1a
Ag film	0	1.7 ± 0.2b	2.9 ± 0.8b	3.5 ± 1.2b	4.8 ± 1.2b	5.6 ± 1.2b	6.1 ± 2.4b
Zn film	0	1.8 ± 0.6b	2.1 ± 0.9b	2.6 ± 1.0b	3.6 ± 1.0b	3.4 ± 1.2b	4.5 ± 1.3b
AgCuZn film	0	0.7 ± 0.1c	0.8 ± 0.1c	1.0 ± 0.1c	1.1 ± 0.2c	1.3 ± 0.2c	1.5 ± 0.4c
Cu particles	0	5.8 ± 1.2a	7.7 ± 1.8a	10.9 ± 1.8a	18.5 ± 2.8a	25.7 ± 5.3a	28.8 ± 4.8a
Ag particles	0	0.9 ± 0.1c	0.9 ± 0.5c	1.1 ± 0.4c	1.5 ± 0.3c	1.5 ± 0.1c	1.5 ± 0.3c
Zn particles	0	0.7 ± 0.1c	0.9 ± 0.2c	1.3 ± 0.5c	1.5 ± 0.2c	1.7 ± 0.2c	1.7 ± 0.5c
AgCuZn particles	0	0.9 ± 0.2c	0.9 ± 0.4c	1.3 ± 0.2c	1.6 ± 0.5c	1.6 ± 0.2c	1.6 ± 0.3c
Mock	0	0	0	0	0	0	0

3.8. Analysis of intracellular nucleic acid and protein leakage

In the nucleic acid leakage assay, the glass control exhibited an absorbance of OD 0.15. Among the film treatments, the Cu film showed OD 0.19 with no significant difference from the control, whereas the Ag film and Zn film each reached OD 0.23, significantly higher than both

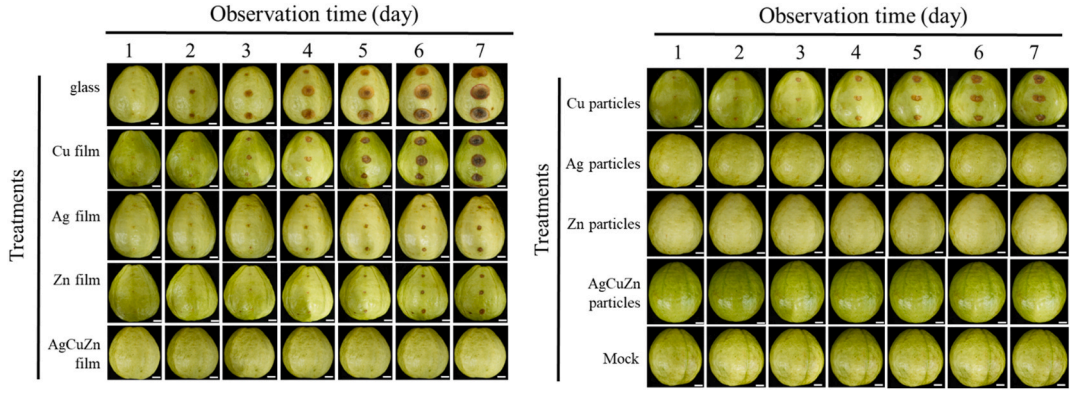

Fig. 5. Lesion development on guava at 1 to 7 days post-inoculation (dpi) with *Pestalotiopsis psidii* conidial suspensions previously contacted with glass, Cu, Ag, Zn, and AgCuZn films or nanoparticles. Mock, sterile-water inoculation. Scale bar = 1 cm.

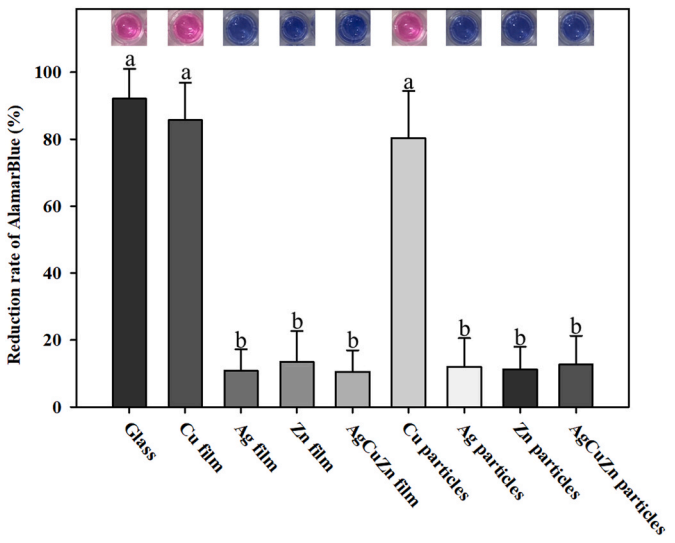

Fig. 6. AlamarBlue reduction in *Pestalotiopsis psidii* after exposure to glass, Cu, Ag, Zn, and AgCuZn films or nanoparticles. Values are presented as mean ± standard deviation (n = 3). Data were analyzed by one-way ANOVA followed by Tukey's HSD post-hoc test. Within each treatment, means that share the same letter are not significantly different ($p < 0.05$).

the control sample and the Cu film. Among all the metal films, the AgCuZn film showed the highest absorbance value of OD 0.32. In the particle groups, the Cu particles showed an absorbance of OD 0.18 (not significantly different from the control), while the Ag and Zn particles yielded OD values of 0.24 and 0.25, respectively, both of which were significantly higher than those of the control sample and Cu particles. Again, the AgCuZn particles showed the highest absorbance value of OD 0.33 (Fig. 8). In the protein leakage assay, the glass control yielded an OD of 0.08. Among the films, the Cu, Ag, and Zn films exhibited optical densities (OD) of 0.12, 0.15, and 0.16, respectively. Although no significant differences were observed among the three films, the Ag and Zn films were significantly different from the control. The AgCuZn film achieved an OD of 0.24, the highest among all the film treatments. Among the dewetted samples, the Cu, Ag, and Zn particles yielded OD values of 0.13, 0.18, and 0.17, respectively, with the Ag and Zn particles showing significantly higher values than the control. The AgCuZn particles again showed the highest value (OD 0.24), which was significantly greater than that of the control and the other particle treatments.

Collectively, the cytoplasmic leakage assays revealed that the Ag-, Zn-, and AgCuZn-based treatments significantly increased the OD260 and OD280 values relative to those of the glass control and Cu treatments. This finding shows that the treatments prompted a more pronounced extracellular release of nucleic acids and proteins, indicating greater membrane damage. The AgCuZn films and particles exhibited the highest absorbance values, suggesting the strongest membrane disruption capacity. Silver and zinc nanomaterials are known to damage cell membranes through multiple mechanisms, including disruption of the membrane proteins and phospholipid bilayer stability, and alteration of the membrane potential and permeability. Alloy materials may further enhance this effect via intermetallic synergism, imposing multiple stresses on cells. Similar phenomena have been reported for CEO-MSNPs, which induce leakage of fungal cell components and soluble sugars [31,32]. The Cu film and particle treatments resulted in slightly increased OD values but showed no significant differences from the control, indicating comparatively weak effects of Cu treatment on the membrane integrity.

3.9. Scanning electron microscopy (SEM) observation of conidial surface morphology after material treatments

In the Cu film group, only partial breakage of the apical appendages was observed. Localized deformation occurred at the distal cells (red arrows), but most of the conidial bodies retained their structural integrity (Fig. 9). However, after Ag film treatment, the apical appendages were markedly curled and deformed. Additionally, the distal appendages were broken, and a collapse of the terminal cell was observed (red arrows). Zn film treatment resulted in breakage of both the apical and distal appendages, accompanied by severe shrinkage and invagination of the distal cells (red arrows), indicating a higher degree of structural damage. The conidia exposed to the AgCuZn alloy film showed extensive breakage of all the appendages, together with rupture of the mid-cell region with cytoplasmic leakage (blue arrows), and the overall collapse and severe deformation of the conidial body. For the particle treatments, the Cu particles primarily caused appendage breakage with mild wrinkling of the apical cell (red arrows), while the remaining conidial body remained relatively intact. The Ag and Zn particles similarly induced appendage breakage, with only minor shrinkage of the distal cells on both sides (red arrows). By contrast, the AgCuZn particles produced pronounced morphological disruption. Beyond appendage breakage, both the apical cells and distal cells exhibited structural rupture with evident cytoplasmic extrusion (blue arrows), suggesting a strong impact on the cell membrane integrity.

Overall, the SEM observations show that the metallic treatments exerted variable effects on the external structure of the *P. psidii* conidia, with the AgCuZn alloy causing the most severe morphological disruption. This finding is consistent with previous reports that Ag nanoparticles disrupt the fungal cell wall architecture, leading to swelling, cytoplasmic leakage, and functional collapse, and Cu nanoparticles compromise the cell envelope integrity in other pathogenic fungi [33]. Together, the results suggest that the potent antifungal activity of alloy films and particles is largely attributable to direct disruption of the cell wall integrity and the subsequent interference with the osmotic balance, indicating that morphological destruction is a key mechanism contributing to antifungal activity [33].

3.10. Fluorescence staining analysis of oxidative stress responses in conidia after metal treatments

The conidia exposed to the glass control showed no green fluorescence, indicating negligible intracellular ROS accumulation under natural conditions (Fig. 10). The conidia treated with the Cu film also showed no green fluorescence, suggesting that the treatment exerted only limited effects on the oxidative stress. However, approximately half of the conidia exposed to the Ag film showed mild green fluorescence (red arrows), reflecting the onset of ROS accumulation in a subset of the cells. Zn film treatment resulted in green fluorescence in more than half of the conidia (red arrows) with a slightly higher intensity than that of Ag films, pointing to a stronger but still moderate induction of ROS. In the AgCuZn film group, most of the conidia exhibited distinct and intense green fluorescence (red arrows) with a broad distribution and stable signal intensity. This pronounced elevation of the intracellular ROS is likely attributable to synergistic interactions among the multiple metals within the alloy, which produce a composite oxidative stress that enhances ROS induction. A similar pattern was observed in the particle treatments. The Cu particles produced no detectable green fluorescence, consistent with the Cu film results and suggesting a non-oxidative-stress mechanism. In contrast, about half of the Ag-treated conidia fluoresced with moderate intensity, while more than half of the Zn-treated conidia showed stronger signals. The AgCuZn particles caused the most pronounced effect, with nearly all the conidia exhibiting intense and uniform fluorescence (red arrows).

Overall, the SEM observations demonstrate that the metallic treatments exert variable effects on the external structure of the *P. psidii*

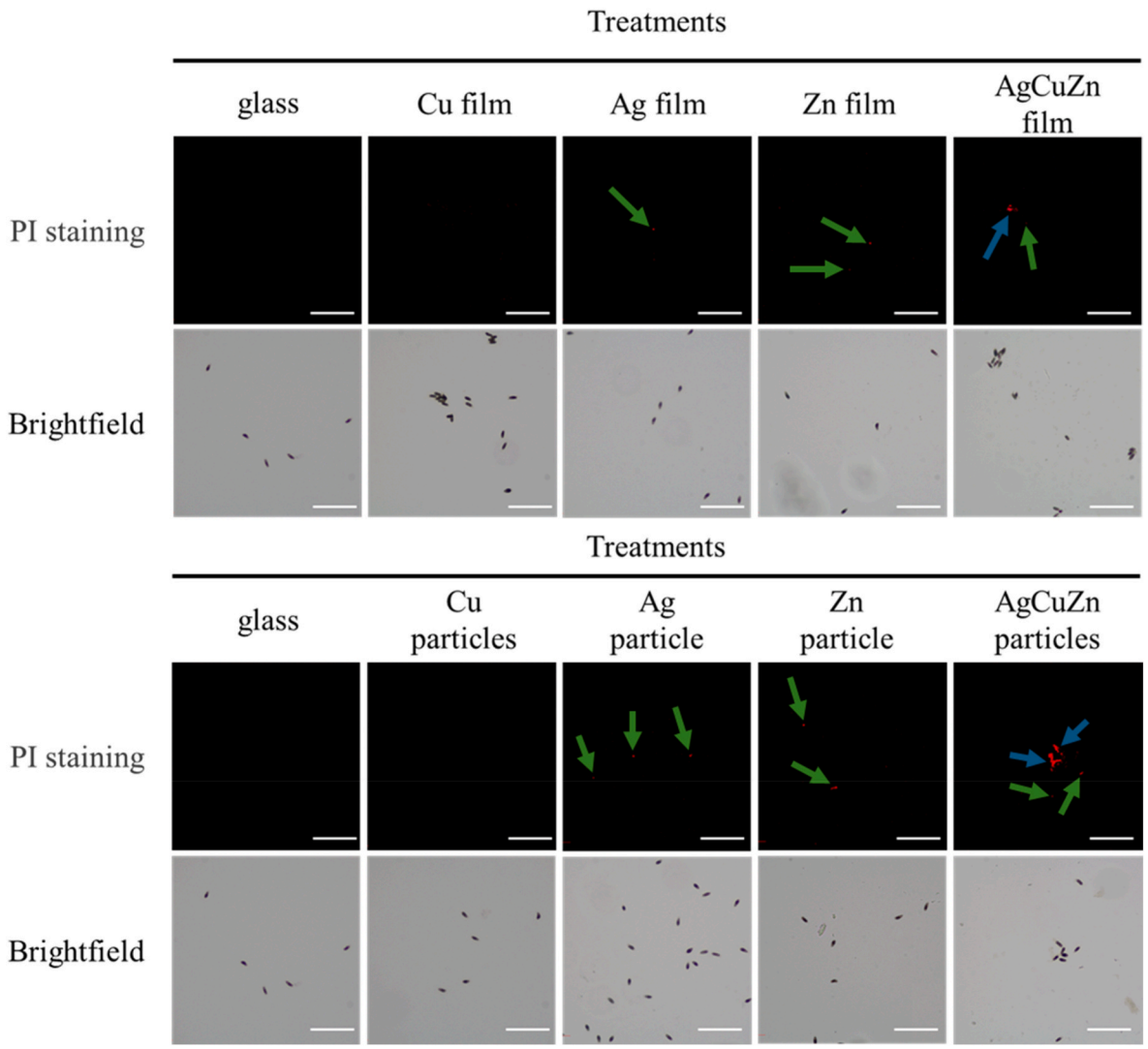

Fig. 7. Propidium iodide (PI) fluorescence staining of *Pestalotiopsis psidii* conidial suspensions after contact with glass, Cu, Ag, Zn, and AgCuZn films or nanoparticles. Green arrows indicate red fluorescence observed inside the cells, while blue arrows indicate red fluorescence detected outside the cells. Scale bar = 10 μm. (For interpretation of the references to colour in this figure legend, the reader is referred to the Web version of this article.)

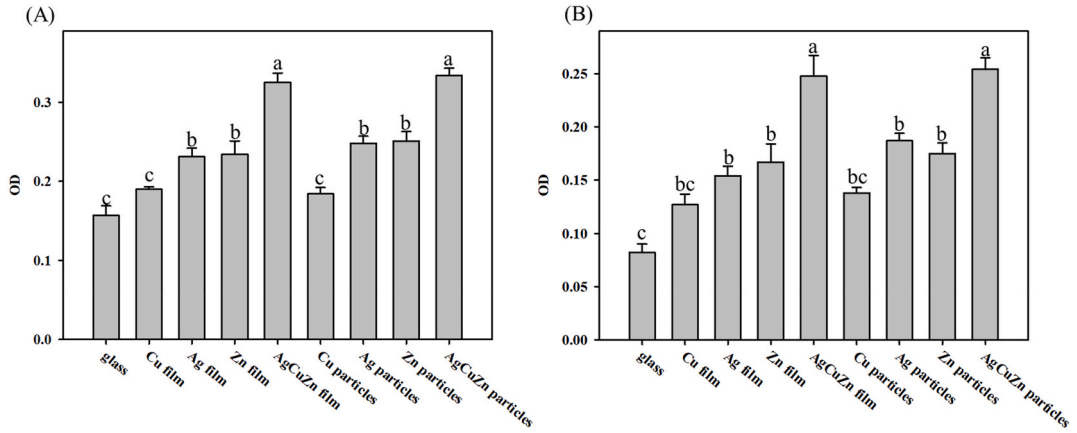

Fig. 8. Cytoplasmic leakage from *Pestalotiopsis psidii* conidia after 30 min exposure to glass, Cu, Ag, Zn, and AgCuZn films or nanoparticles. (A) Nucleic-acid leakage ($O.D._{260}$). (B) Protein leakage ($O.D._{280}$). Values are expressed as mean ± standard deviation (n = 3). Data were analyzed by one-way ANOVA followed by Tukey's HSD test. Within each treatment, means that share the same letter are not significantly different ($p < 0.05$).

conidia, with the AgCuZn treatments producing the strongest effect. This aligns with previous reports indicating that Ag and Zn nanomaterials

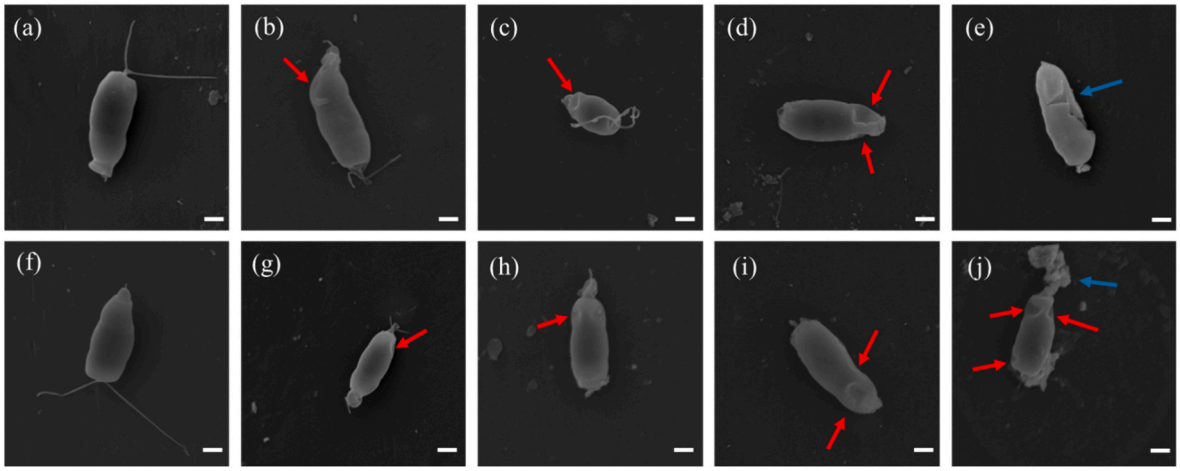

Fig. 9. Scanning electron micrographs of *Pestalotiopsis psidii* conidia after 10 min contact with glass, Cu, Ag, Zn, and AgCuZn films or nanoparticles. Scale bar = 2 μm. Red arrows indicate surface shrinkage of the conidia, while blue arrows indicate ruptures in the cell wall. (a, f) Control (glass); (b–e) thin films of (b) Cu, (c) Ag, (d) Zn, and (e) AgCuZn; (g–j) laser-dewetted nanoparticles of (g) Cu, (h) Ag, (i) Zn, and (j) AgCuZn. (For interpretation of the references to colour in this figure legend, the reader is referred to the Web version of this article.)

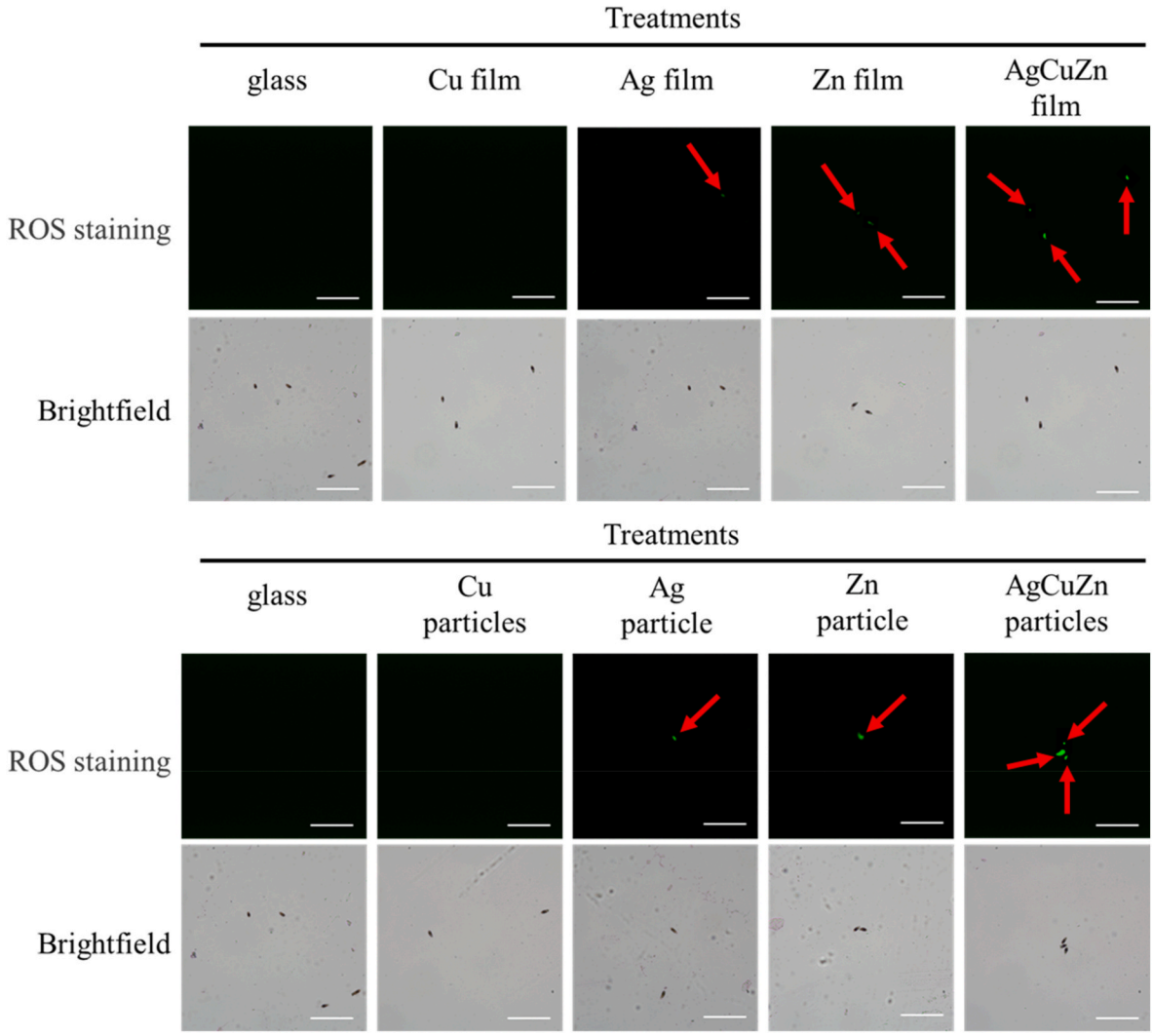

Fig. 10. Reactive-oxygen-species (ROS) fluorescence in *Pestalotiopsis psidii* conidial suspensions stained with cell-permeable probe 2′,7′-dichlorodihydrofluorescein diacetate (DCFH-DA) and then exposed for 10 min to glass, Cu, Ag, Zn, and AgCuZn films or nanoparticles. Increased green fluorescence indicates intracellular ROS accumulation. Red arrows indicate areas of observed green fluorescence. Scale bar = 10 μm. (For interpretation of the references to colour in this figure legend, the reader is referred to the Web version of this article.)

exert antimicrobial effects mainly through excessive ROS generation (e.g., superoxide anions, hydroxyl radicals, and hydrogen peroxide), which damages membranes, mitochondria, and DNA and can trigger apoptosis [6,34]. Silver and zinc nanoparticles are further known to disrupt the membrane potential and impair antioxidant enzyme activity, thereby elevating the oxidative stress [7,35]. Chen et al. [36,37] also reported that Pd-HA NPs directly caused cancer cell death by producing highly toxic reactive oxygen therapy (ROS) through chemodynamic therapy (CDT). The strong green fluorescence observed in the conidia treated with Ag, Zn, and AgCuZn thus reflects an oxidative-stress-mediated antifungal mechanism, supporting the role of these materials as ROS-driven antifungal agents.

4. Conclusion

This study evaluated the antifungal efficacy and potential mechanisms of Cu, Ag, Zn, and AgCuZn thin films and nanoparticles against the guava scab pathogen *Pestalotiopsis psidii*. The antifungal performance of the materials was assessed through colony inhibition assays, conidial germination tests, and fruit inoculation experiments. The mechanistic investigations included intracellular ROS accumulation, membrane integrity analysis, cytoplasmic leakage, and morphological observations. Together, these approaches enabled a comprehensive comparison of the antifungal behaviors and underlying pathways of the different metallic materials. With respect to the antifungal efficacy, the Ag, Zn, and AgCuZn treatments exhibited a pronounced and rapid inhibitory activity. In the plate assay, these treatments completely suppressed colony formation within 15 min of contact with the cells. By contrast, the Cu treatment achieved only ~60–70% inhibition after 30 min. A similar trend was observed in the germination assays. In particular, after 24 h of incubation, the conidial germination rate remained at only 23.1–27.3% for the Ag-, Zn-, and AgCuZn-treated samples but increased to 85.0% and 59.1% for the glass control and Cu-treated groups, respectively. These findings indicate that Ag, Zn, and AgCuZn markedly delay or prevent spore germination, thereby suppressing the potential for early-stage infection. The inoculation assays provided further confirmation of their potent antifungal activity: no lesion development or typical symptoms of *P. psidii* were observed in the Ag-, Zn-, and AgCuZn-treated fruits, and the pathogen could not be re-isolated from the wound tissues, indicating a successful interruption of the infection cycle. In contrast, Cu treatment delayed symptom progression but produced evident lesions by day seven, showing that Cu achieved only a limited inhibitory capacity.

The mechanistic analyses revealed that the potent activity of Ag, Zn, and AgCuZn was closely associated with the strong induction of intracellular ROS. DCFH-DA fluorescence staining showed marked green signals in the conidia treated with these materials, most prominently and uniformly in the AgCuZn group, indicating significant oxidative stress. In contrast, the Cu-treated conidia showed no appreciable ROS accumulation and remained non-fluorescent blue, indicating a non-oxidative mechanism. Propidium iodide staining and cytoplasmic leakage assays confirmed ROS-related membrane damage. Conidia treated with Ag, Zn, and AgCuZn exhibited strong red fluorescence and extracellular signals, indicating membrane rupture and nucleic acid release. The OD260 and OD280 measurements supported these findings, showing significant increases in DNA/RNA and protein leakage, respectively, particularly in the AgCuZn group. The SEM observations confirmed that the AgCuZn-treated conidia exhibited broken appendages, ruptured mid-cell regions, and cytoplasmic extrusion, highlighting ROS-mediated membrane and structural breakdown as the main destructive pathway. Although the Cu materials exhibited favorable fabrication properties and thermal stability, their overall antifungal activity was markedly weaker than that of the other materials. They failed to induce ROS generation and rupture the membrane integrity, and yielded only mild conidial deformation. This suggests that Cu operates primarily through alternative, non-ROS pathways, such as Cu ion release or interaction with extracellular membrane proteins to inhibit energy metabolism, which differs fundamentally from the ROS-dependent mechanisms of the Ag, Zn, and AgCuZn materials.

Overall, the present findings demonstrate that Ag, Zn, and AgCuZn materials outperform Cu in antifungal efficacy, mechanism, and stability, effectively inhibiting *P. psidii* germination and pathogenicity within a short timeframe. The key mode of action of these materials involves the rapid induction of intracellular ROS, which leads to membrane disruption, cytoplasmic leakage, and structural collapse. Among the considered materials, the AgCuZn film and particles exhibited the highest ROS-inducing and inhibitory capacities owing to synergistic metallic effects. By contrast, the Cu materials acted mainly via non-oxidative pathways and exerted only partial inhibition. From an application standpoint, the Ag, Zn, and AgCuZn nanomaterials could be developed into foliar sprays, post-harvest coatings, or slow-release formulations, providing eco-friendly alternatives to conventional fungicides in guava cultivation.

CRediT authorship contribution statement

H.K. Lin: Writing – review & editing, Writing – original draft, Supervision, Resources, Funding acquisition, Conceptualization. **Min-Yang Chen:** Writing – original draft, Methodology, Investigation, Data curation, Conceptualization. **Po-Wei Chang:** Visualization, Methodology, Investigation, Formal analysis, Data curation. **Ya-Zhen Xu:** Methodology, Data curation. **Ying-Hong Lin:** Writing – original draft, Supervision, Formal analysis, Conceptualization.

Declaration of competing interest

The authors declare that they have no known competing financial interests or personal relationships that could have appeared to influence the work reported in this paper.

Acknowledgements

The authors gratefully acknowledge the financial support provided to this study by the National Science and Technology Council, ROC, under Project No. NSTC 114-2221-E-020-016.

Data availability

Data will be made available on request.

References

[1] F. Solarte, C.G. Muñoz, S.S. Maharachchikumbura, E. Álvarez, Diversity of Neopestalotiopsis and Pestalotiopsis spp., causal agents of guava scab in Colombia, Plant Dis. 102 (1) (2018) 49–59.
[2] L.M. Keith, M.E. Velasquez, F.T. Zee, Identification and characterization of pestalotiopsis spp. causing scab disease of guava, Psidium guajava, in Hawaii, Plant Dis. 90 (1) (2006) 16–23.
[3] A.K. Rao, A.A. Lal, S.D. Simon, S. Chandra, R.K. Singh, L. Singh, Management of canker (Pestalotia psidii) disease of Guava (Psidium guajava L.), Ann. Plant Protect. Sci. 20 (2012) 383–385.
[4] V.I. Lushchak, T.M. Matviishyn, V.V. Husak, J.M. Storey, K.B. Storey, Pesticide toxicity: a mechanistic approach, EXCLI J. 17 (2018) 1101–1136.
[5] Y.-H. Lin, J.-J. Wang, Y.-T. Wang, H.-K. Lin, Y.-J. Lin, Antifungal properties of pure silver films with nanoparticles induced by pulsed-laser dewetting process, Appl. Sci. (2020).
[6] A. Carrapiço, M.R. Martins, A.T. Caldeira, J. Mirão, L. Dias, Biosynthesis of metal and metal oxide nanoparticles using microbial cultures: mechanisms, antimicrobial activity and applications to cultural heritage, Microorganisms 11 (2) (2023) 378.
[7] S.P. Theofilou, C. Antoniou, L. Potamiti, A. Hadjisavvas, M. Panayiotidis, P. G. Savva, C. Costa, V. Fotopoulos, Immobilized Ag-nanoparticles (iNPs) for environmental applications: elucidation of immobilized silver-induced inhibition mechanism of Escherichia coli, J. Environ. Chem. Eng. 9 (5) (2021) 106001.
[8] T. Shen, Q. Wang, C. Li, B. Zhou, Y. Li, Y. Liu, Transcriptome sequencing analysis reveals silver nanoparticles antifungal molecular mechanism of the soil fungi Fusarium solani species complex, J. Hazard. Mater. 388 (2020) 122063.
[9] M.S. Madhuri Sharon, A.K. Choudhary, R.K. Rohit Kumar, Nanotechnology in agricultural diseases and food safety, J. Phytol. 2 (4) (2010) 78–82.

[10] M. Gajbhiye, J. Kesharwani, A. Ingle, A. Gade, M. Rai, Fungus-mediated synthesis of silver nanoparticles and their activity against pathogenic fungi in combination with fluconazole, Nanomed. Nanotechnol. Biol. Med. 5 (4) (2009) 382–386.
[11] K.S. Iliger, T.A. Sofi, N.A. Bhat, F.A. Ahanger, J.C. Sekhar, A.Z. Elhendi, A.A. Al-Huqail, F. Khan, Copper nanoparticles: green synthesis and managing fruit rot disease of chilli caused by Colletotrichum capsici, Saudi J. Biol. Sci. 28 (2) (2021) 1477–1486.
[12] H. Chhipa, Nanofertilizers and nanopesticides for agriculture, Environ. Chem. Lett. 15 (1) (2017) 15–22.
[13] T.L. Meister, J. Fortmann, M. Breisch, C. Sengstock, E. Steinmann, M. Köller, S. Pfaender, A. Ludwig, Nanoscale copper and silver thin film systems display differences in antiviral and antibacterial properties, Sci. Rep. 12 (1) (2022) 7193.
[14] C.P. Randall, A. Gupta, N. Jackson, D. Busse, A.J. O'Neill, Silver resistance in Gram-negative bacteria: a dissection of endogenous and exogenous mechanisms, J. Antimicrob. Chemother. 70 (4) (2015) 1037–1046.
[15] M. Kaushal, S. Indoria, T.S. Lobana, H. Sood, D.S. Arora, G. Hundal, V.A. Smolinski, M. Kaur, J.P. Jasinski, Synthesis, structures and antimicrobial activity of 5-nitro-salicylaldehyde-thiosemicarbazonates of zinc (II) coordinated to substituted bipyridines/phenanthrolines, Polyhedron 148 (2018) 9–21.
[16] K. Alomar, A. Landreau, M. Kempf, M.A. Khan, M. Allain, G. Bouet, Synthesis, crystal structure, characterization of zinc(II), cadmium(II) complexes with 3-thiophene aldehyde thiosemicarbazone (3TTSCH). Biological activities of 3TTSCH and its complexes, J. Inorg. Biochem. 104 (4) (2010) 397–404.
[17] N.C. Kasuga, K. Sekino, M. Ishikawa, A. Honda, M. Yokoyama, S. Nakano, N. Shimada, C. Koumo, K. Nomiya, Synthesis, structural characterization and antimicrobial activities of 12 zinc(II) complexes with four thiosemicarbazone and two semicarbazone ligands, J. Inorg. Biochem. 96 (2) (2003) 298–310.
[18] M.C. Rodríguez-Argüelles, P. Tourón-Touceda, R. Cao, A.M. García-Deibe, P. Pelagatti, C. Pelizzi, F. Zani, Complexes of 2-acetyl-γ-butyrolactone and 2-furancarbaldehyde thiosemicarbazones: antibacterial and antifungal activity, J. Inorg. Biochem. 103 (1) (2009) 35–42.
[19] A. Ragab, Y.A. Ammar, A. Ezzat, A.M. Mahmoud, M.B.I. Mohamed, A.S. El-Tabl, R. S. Farag, Synthesis, characterization, thermal properties, antimicrobial evaluation, ADMET study, and molecular docking simulation of new mono Cu (II) and Zn (II) complexes with 2-oxoindole derivatives, Comput. Biol. Med. 145 (2022) 105473.
[20] K.-H. Huynh, X.-H. Pham, J. Kim, S.H. Lee, H. Chang, W.-Y. Rho, B.-H. Jun, Synthesis, properties, and biological applications of metallic alloy nanoparticles, Int. J. Mol. Sci. 21 (14) (2020) 5174.
[21] J.J. Wang, H.K. Lin, W.S. Chuang, C.Y. Chuang, Y.-H. Lin, J.C. Huang, Y.-H. Lin, Laser dewetting mechanism and antibacterial properties of Cu-Al based medium entropy alloy films, J. Alloys Compd. 903 (2022) 163893.
[22] H.-K. Lin, S.-J. Yang, P.-W. Chang, W.-H. Lu, Y.-J. Chang, Effects of laser patterning and heat treatment on hydrophobicity, wear, and corrosion resistance of 316L stainless steel, Int. J. Adv. Manuf. Technol. 137 (11) (2025) 5511–5520.
[23] Y.-F. Yan, C.-J. Yang, X.-F. Shang, Z.-M. Zhao, Y.-Q. Liu, R. Zhou, H. Liu, T.-L. Wu, W.-B. Zhao, Y.-L. Wang, G.-F. Hu, F. Qin, Y.-H. He, H.-X. Li, S.-S. Du, Bioassay-guided isolation of two antifungal compounds from Magnolia officinalis, and the mechanism of action of honokiol, Pestic. Biochem. Physiol. 170 (2020) 104705.
[24] Y. Wu, J.-H. Cheng, D.-W. Sun, Subcellular damages of Colletotrichum asianum and inhibition of mango anthracnose by dielectric barrier discharge plasma, Food Chem. 381 (2022) 132197.
[25] E. Rio, A. Daerr, L. Limat, Probing with a laser sheet the contact angle distribution along a contact line, J. Colloid Interface Sci. 269 (1) (2004) 164–170.
[26] R.I. Shebl, F. Farouk, H.M.E.-S. Azzazy, Effect of surface charge and hydrophobicity modulation on the antibacterial and antibiofilm potential of magnetic iron nanoparticles, J. Nanomater. 2017 (1) (2017) 3528295.
[27] Y. Duan, J. Yu, Improving reactive oxygen species generated from micro-nano bubbles by hydrophobic catalytic ceramic membrane for wastewater treatment, Chem. Eng. J. 500 (2024) 157206.
[28] S. Parveen, A.H. Wani, M.A. Shah, H.S. Devi, M.Y. Bhat, J.A. Koka, Preparation, characterization and antifungal activity of iron oxide nanoparticles, Microb. Pathog. 115 (2018) 287–292.
[29] A.F. Oussou-Azo, T. Nakama, M. Nakamura, T. Futagami, M.d.C.M. Vestergaard, Antifungal potential of nanostructured crystalline copper and its oxide forms, Nanomaterials (2020).
[30] K.-J. Kim, W.S. Sung, B.K. Suh, S.-K. Moon, J.-S. Choi, J.G. Kim, D.G. Lee, Antifungal activity and mode of action of silver nano-particles on Candida albicans, Biometals 22 (2) (2009) 235–242.
[31] V.K. Bajpai, A. Sharma, K.-H. Baek, Antibacterial mode of action of Cudrania tricuspidata fruit essential oil, affecting membrane permeability and surface characteristics of food-borne pathogens, Food Control 32 (2) (2013) 582–590.
[32] R. Zhang, Y. Cui, M. Cheng, Y. Guo, X. Wang, J. Wang, Antifungal activity and mechanism of cinnamon essential oil loaded into mesoporous silica nanoparticles, Ind. Crop. Prod. 171 (2021) 113846.
[33] E. Ibrahim, J. Luo, T. Ahmed, W. Wu, C. Yan, B. Li, Biosynthesis of silver nanoparticles using onion endophytic bacterium and its antifungal activity against rice pathogen magnaporthe oryzae, J. Fungi (2020).
[34] G.D. Savi, A.J. Bortoluzzi, V.M. Scussel, Antifungal properties of Zinc-compounds against toxigenic fungi and mycotoxin, Int. J. Food Sci. Technol. 48 (9) (2013) 1834–1840.
[35] U. Kadiyala, E.S. Turali-Emre, J.H. Bahng, N.A. Kotov, J.S. Vanepps, Unexpected insights into antibacterial activity of zinc oxide nanoparticles against methicillin resistant staphylococcus aureus (MRSA), Nanoscale 10 (10) (2018) 4927–4939.
[36] X. Chen, Z. Jia, Y. Wen, Y. Huang, X. Yuan, Y. Chen, Y. Liu, J. Liu, Bidirectional anisotropic palladium nanozymes reprogram macrophages to enhance collaborative chemodynamic therapy of colorectal cancer, Acta Biomater. 151 (2022) 537–548.
[37] X. Chen, Y. Yang, J. Chen, Y. He, Y. Huang, Q. Huang, W. Deng, R. Zhu, X. Huang, T. Li, Dual-driven selenium Janus single-atom nanomotors for autonomous regulating mitochondrial oxygen imbalance to catalytic therapy of rheumatoid arthritis, Redox Biol. 81 (2025) 103574.